Rapid #: -21251019

CROSS REF ID: **718866**

LENDER: **COF (Colorado State University) :: Morgan Library**

BORROWER: **DXU (Drexel University) :: Hagerty Library**

TYPE:	Article CC:CCG
JOURNAL TITLE:	Desalination
USER JOURNAL TITLE:	Desalination
ARTICLE TITLE:	A new static mixer concept for enhanced desalination performance in flow-electrode capacitive deionization (FCDI) systems
ARTICLE AUTHOR:	Ehring, Jonathan C
VOLUME:	566
ISSUE:	
MONTH:	
YEAR:	2023
PAGES:	116887-
ISSN:	0011-9164
OCLC #:	38871433

Processed by RapidX: 9/11/2023 2:51:17 PM

Desalination 566 (2023) 116887

Contents lists available at ScienceDirect

Desalination

journal homepage: www.elsevier.com/locate/desal

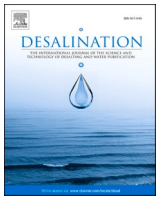

A new static mixer concept for enhanced desalination performance in flow-electrode capacitive deionization (FCDI) systems

Jonathan C. Ehring [a], Ali Vala Mizrak [a], Lutfi Agartan [a], Bilen Aküzüm [b], E. Caglan Kumbur [a,*]

[a] Electrochemical Energy Systems Laboratory, Department of Mechanical Engineering and Mechanics, Drexel University, Philadelphia, PA 19104, USA
[b] Energy Storage and Distributed Resources Division, Lawrence Berkeley National Laboratory, Berkeley, CA 94720, USA

HIGHLIGHTS

- A new static mixer design is proposed for low carbon loading slurries (<2 wt%).
- The MASM flow field improved ASRR by 250 % compared to baseline flow field.
- EIS results suggest charge transfer occurs at the current collector-IEM interface.
- 90-min desalination tests showed 3× more salt removal than the baseline flow field.

ARTICLE INFO

Keywords:
Flow-capacitive deionization
FCDI
Static mixer
Flowable electrodes
Membrane

ABSTRACT

Poor electrical conductivity and high pumping energy cost are two major challenges that limit the desalination performance of flow-electrode capacitive deionization (FCDI) systems. In this study, we address these limitations by utilizing low carbon loading suspensions (≤2 wt%) with water-like viscosity in a novel static mixer design, referred to as a membrane-assisted static mixer (MASM). MASMs improved the electrical conductivity of the slurry by minimizing the charge transport distances between the active material and current collector as the ion-exchange membrane was compressed directly against the current collector surface (i.e., zero-gap flow field). Continuous mixing of the active material was achieved by controlling the displacement of the membrane via pressure fluctuations from the peristaltic pumps. A parametric study of three MASM flow field geometries was performed at varying flow rates of 1, 3, 5, 10, 15 and 25 mL min^{-1} and 0.5, 1, and 2 wt% activated carbon (AC). The best-performing flow configuration (2 wt% AC and 15 mL min^{-1}) showed a high salt removal rate of 4.424 μg NaCl cm^{-2} s^{-1} with a total energy consumption of 98.95 kJ mol^{-1}.

1. Introduction

The availability of freshwater is becoming an increasingly pressing issue as climate change and groundwater depletion continue to harm reservoirs worldwide [1]. Desalination technologies such as reverse osmosis, multi-stage flash and salt water evaporation are some of the most popular desalination technologies, where reverse osmosis (RO) is widely considered the most efficient desalination technology for salt water concentrations [2]. However, RO technologies are less efficient at lower salt concentrations and could potentially be supplemented by a secondary stage of desalination [3] using emerging technologies such as capacitive deionization (CDI) and flow electrode capacitive deionization (FCDI).

CDI is an electrically driven method of removing dissolved salt ions from salt or brackish water feed streams by pumping the feed solution between polarized electrodes separated by an ion-exchange membrane (IEM). The salt ions in the feed stream are adsorbed onto the porous carbon surface via the electric double layer (EDL) [4] which is driven by an external power supply of typically 1.2 V or less. CDI is an attractive method of desalination because it is more energy efficient in terms of pressure and pumping requirements, and more efficiently removes ions from the waste stream [5,6] with energy consumption values <1 kWh m^3 at brackish water salt concentrations (2 g L^{-1} NaCl) [7]. However, ion saturation of the carbon electrodes is a major limitation of CDI systems and requires the system to be discharged before ions can be adsorbed back into the carbon electrodes [8]. An alternative approach is

* Corresponding author.
E-mail address: eck32@drexel.edu (E.C. Kumbur).

https://doi.org/10.1016/j.desal.2023.116887
Received 15 March 2023; Received in revised form 13 July 2023; Accepted 31 July 2023
Available online 4 August 2023

the utilization of slurry electrodes in a FCDI system which avoids ion saturation by continuously replenishing the system with uncharged carbon particles dispersed in the flowable electrode.

Flowable electrodes consist of a biphasic solution of solid particles (electrically conductive) and liquid electrolyte (ionically conductive) that are polarized upon entering the flow field and contacting the current collector. However, in response to the electrode polarization, the ionic species in the feed water channel begin to migrate to the oppositely charged electrodes, passing through the IEMs and getting adsorbed onto the carbon particles via the EDL. Once adsorbed, the counterions in the electrolyte provide coulombic repulsion forces and balance the system. Continual pumping of the slurry removes the charged particles from the cell, which can be pumped through another cell to discharge the particles and release the previously captured ions into a brine stream. While conventional CDI remains superior in terms of the charge transfer kinetics [8], FCDI offers many benefits, including flexible and scalable system designs via external reservoirs that conventional systems cannot offer. The major drawback of FCDI systems is the low electrical conductivity of the slurry electrode due to the continual disruption of the percolation networks [9] and the high pumping energy needed due to hydrodynamic losses [10]. Many recent studies have aimed at improving the electrical conductivity of the flowable electrodes by controlling the formation of percolation networks [11–13], introducing higher capacitance electrode materials [14–17], surface modifications [18], flow field design [19], and the addition of 3D printed static mixers [20].

Percolation networks have seen the most attention as activated carbon (AC) loadings in the range of 10–30 wt% greatly increase the conductivity via long-spanning networks of interlocking particles. However, an often-overlooked consequence of FCDI systems is the energy consumption related to pumping viscous fluids (i.e., frictional losses, pump efficiency, etc.). As such, the investigation of FCDI devices that utilize low-viscosity suspensions while maintaining high electrochemical performance has been the focus of recent research.

Materials-based studies have focused on the use of carbon nanotubes [21], graphene nanoplatelets [11], and other nanomaterials in order to electrically bridge the neighboring activated carbon particles [22]. Small additions of these high aspect ratio nanomaterials enhance electrochemical performance significantly while decreasing the viscosity up to one-fourth of its original value [11]. Other studies have attempted to decrease the viscosity while simultaneously increasing electrical conductivity via an electrostatic repulsion [9], oxidation [23], and ion-selective functional groups [18]. The long-term reliability of these surface modifications is still not completely understood since the particles tend to agglomerate, reduce in size and consequently increase the viscosity of the slurry [24].

At the systems level, 3D printed inserts and static mixers have been shown to increase the flow characteristics of the electrolyte [25] and increase the rate of particle-particle interactions while decreasing charge transport distances [20]. A major drawback of 3D-printed static mixers is the reliability of the conductive coating, which may increase the resistance of the cell over time. Other concerns are related to cost, limited manufacturing at scale, and added complexity of cell design and assembly. Traditional flow fields (i.e., serpentine, interdigitated, etc.) are designed to accommodate suspensions with high carbon loadings which promote the formation of the percolation network and increase the electrical conductivity of the slurry [19]. While some studies have used low carbon loading suspensions to the best of our knowledge, there has not been a flow field specifically designed for low carbon loadings for use in FCDI devices.

Increasing the carbon loading of the suspension is typically seen as the most direct solution to increase salt adsorption; however, optimization of the suspension is still being heavily researched, and it is not clear if higher carbon loadings is the optimal solution. In fact, it may be more efficient and more economical to use lower carbon loading suspensions, which have several benefits, including: water-like viscosity, reduced pressure drop, low frictional losses, low pumping cost, decreased maintenance, reduced equipment wear, and are less prone to channel clogging.

Charge transport theory suggests particles become charged when contacting the current collector, colliding with another charged particle or contacting conductive additive material that is also in contact with the current collector. Several studies have modeled the particle-particle interactions between charged and uncharged particles [26,27] and found that much of the charge transfer occurred at the current collector walls, rather than between particle-particle interactions. This is due to the uneven charge distribution from colliding particles, whereas a particle contacting the current collector becomes fully charged in the process. Therefore, design and optimization of flow fields that promote particle-current collector interactions could potentially increase the slurry conductivity. In this study, we introduce a new static mixer concept for FCDI systems that improves charge transport among low carbon loading suspensions (i.e., less than percolation threshold) by utilizing a zero-gap flow field design focused on particle-current collector interactions, rather than percolation networks to increase conductivity.

In a traditional flow field (Fig. 1a), activated carbon particles flow through a channel and become charged upon contact with the current collector or when colliding with neighboring charged particles. In suspensions below the percolation threshold, particle-particle interactions are less likely to occur and so particles within the flow field become underutilized and lead to decreased performance. One way to increase carbon utilization within the flow field is to decrease the charge transport distance by placing the IEM directly against the flat current collector surface (Fig. 1b). However, a major drawback with a zero-gap flow field design is the reduced residence time of the particles in the flow field, as the flow field volume is significantly lower. This decreased residence time impacts the number of particle-current collector interactions and therefore decreases salt adsorption. To counter this reduction in residence times, the proposed flow field (Fig. 1c) includes channels machined into the back surface (i.e., toward the end plate. See Fig. 2). Given the high flowability of the slurry, carbon particles are able to travel over channel walls and into neighboring channels as the pressure is increased. The displacement of the membrane plays a significant role in the proposed static mixer design as it acts to continuously mix the carbon particles with each pressure cycle.

During its relaxed state, the IEM is compressed against the current collector surface and activated carbon particles are forced into channels that direct flow toward the outlet. At pressure peaks, the increased pressure bulges the membrane away from the current collector surface and carbon particles flow toward the IEM. In this way, the ion-exchange membrane acts as a diaphragm-like device, whereby it contracts and flattens onto the current collector (CC) surface during its relaxed state and bulges away from the CC during pressure peaks. Compression of the membrane pulls the surrounding carbon particles into the machined channels (Fig. 2) and generates particle mixing within the small channels. Once the membrane expands and bulges away from the current collector surface, the carbon particles are drawn to fill the void between the membrane and the current collector. Rather than relying solely upon particle-particle interactions (i.e., percolation networks) to increase conductivity, the MASM concept forces and promotes the particle-current collector interactions to take place at the interface between the IEM and CC where they have the best chance of adsorbing ions. As the pump continues to cyclically vary in pressure, the particles migrate to neighboring channels and eventually to the outlet.

A parametric study of the proposed static mixer design was conducted with varying flow field geometry and current collector surface area, as described in Table 1. The overall goal was to demonstrate and better understand the membrane-assisted mechanism by investigating the effects of flow rate on the average salt removal rate (ASRR), pressure drop, and energy consumption of a lab-scale FCDI system (Fig. 2). This was accomplished by conducting chronoamperometry tests for each flow field across three different weight percentages (0.5, 1, 2 wt%) of

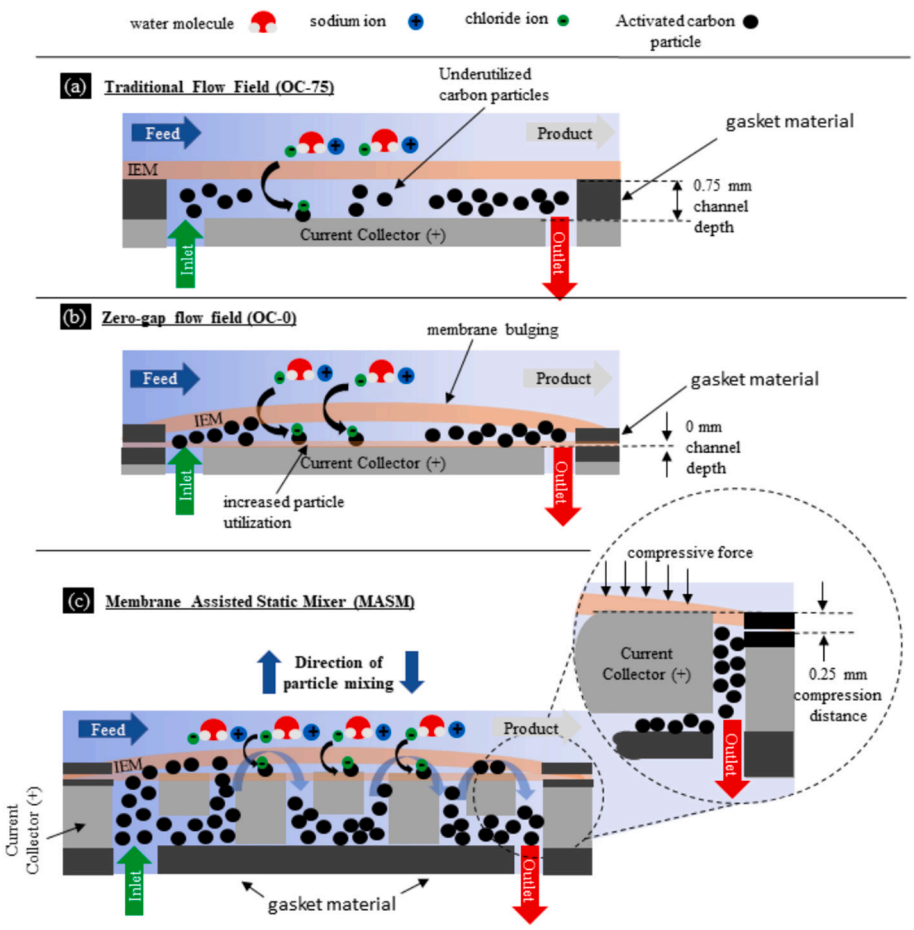

Fig. 1. A comparison of the different types of flow field configurations: (a) traditional open channel flow field, (b) zero-gap flow field and (c) MASM flow field.

activated carbon (AC, Norit SX Ultra) and flow rates of 1, 3, 5, 10, 15, and 25 mL min^{-1}. Pressure drops were recorded for each experiment while desalinating 2 g L^{-1} NaCl feed solution. Energy consumption and ASRR were calculated for each case and plotted to determine the optimal flow rates and AC loading. Desalination performances of two open channel designs were employed as reference values for the tested MASM cases. Additionally, electrochemical impedance spectroscopy (EIS) was conducted under the best-performing conditions to better understand the relationships between the flow field geometry and the electrical conductivity. Lastly, long-term desalination tests were conducted over a 90-min period to demonstrate the reliability of the MASM design.

2. Materials and methods

2.1. Materials and FCDI setup

In this study, 25 mL of slurry was prepared by first combining 3.5 wt % sodium chloride (NaCl; powder, Sigma Aldrich, USA), 0.5 wt% carbon black (conductive additive; 100 % compressed, Alfa Aesar, USA), and varying weight percentages (0.5, 1, 2 wt%) of activated carbon (Norit® SX ultra; powder, Sigma Aldrich, USA). The slurries were mixed using a magnetic stirrer for 10 min, followed by shear mixing (IKA T-18 Ultra Turrax Digital Homogenizer) at 20,000 rpm for 5 min. Graphite plates were machined using a tabletop MicroMill DSLS 3000 CNC according to the dimensions given in Fig. 2c, e and Table 1 and were designated as MASM-x, where x represents the number of discrete channels in the flow field. Similarly, the open channel was designed with the same flow field dimensions (25 mm × 75 mm) but with depths of 0 mm (OC-0) and 0.75 mm (OC-75). OC-0 was chosen to check/validate the membrane-assisted mechanism, while OC-75 was used as a comparison to more traditional flow fields. Sandwiched between the two symmetric flow fields was the water channel consisting of three gaskets with an overall depth of 2 mm. Lastly, the IEMs were compressed directly onto the current collector surface to reduce charge transfer distances and promote fluid flow toward the IEM. No noticeable side effects, such as tearing or reduced ion transfer, were observed during or after compression.

2.2. Membrane-assisted static mixer (MASM) design considerations

Compression of the membrane against the current collector surface was a critical factor in ensuring the membrane bulged and flattened during pressure peaks and valleys. To achieve this, the membrane was compressed against the current collector surface by removing the graphite material surrounding the flow field to a depth of 1 mm and placed onto a rubber gasket with a thickness of 0.75 mm, yielding a compression distance of 0.25 mm (Fig. 1c). In this way, the membrane was flattened onto the current collector surface, and the compressive force was finely adjusted according to the torque applied to the cell bolts. Tightening the bolts above 10 Nm of torque showed high pressures and poor electrochemical performance, indicating that the membrane failed to bulge from the current collector. Likewise, tightening the bolts below 7 Nm of torque led to cell leakage. Therefore, the cell bolts were tightened to approximately 8 Nm of torque to prevent leakage and to enable the membrane bulging action.

The channels machined into the current collector functioned to store the carbon particles and increase their residence time within the flow field. Given the high flowability of the slurry, the motion of the membrane sufficiently mixed the particles within the channels and enhanced the particle–current collector interactions. However, the quality of particle mixing and the rate of particle–current collector interactions

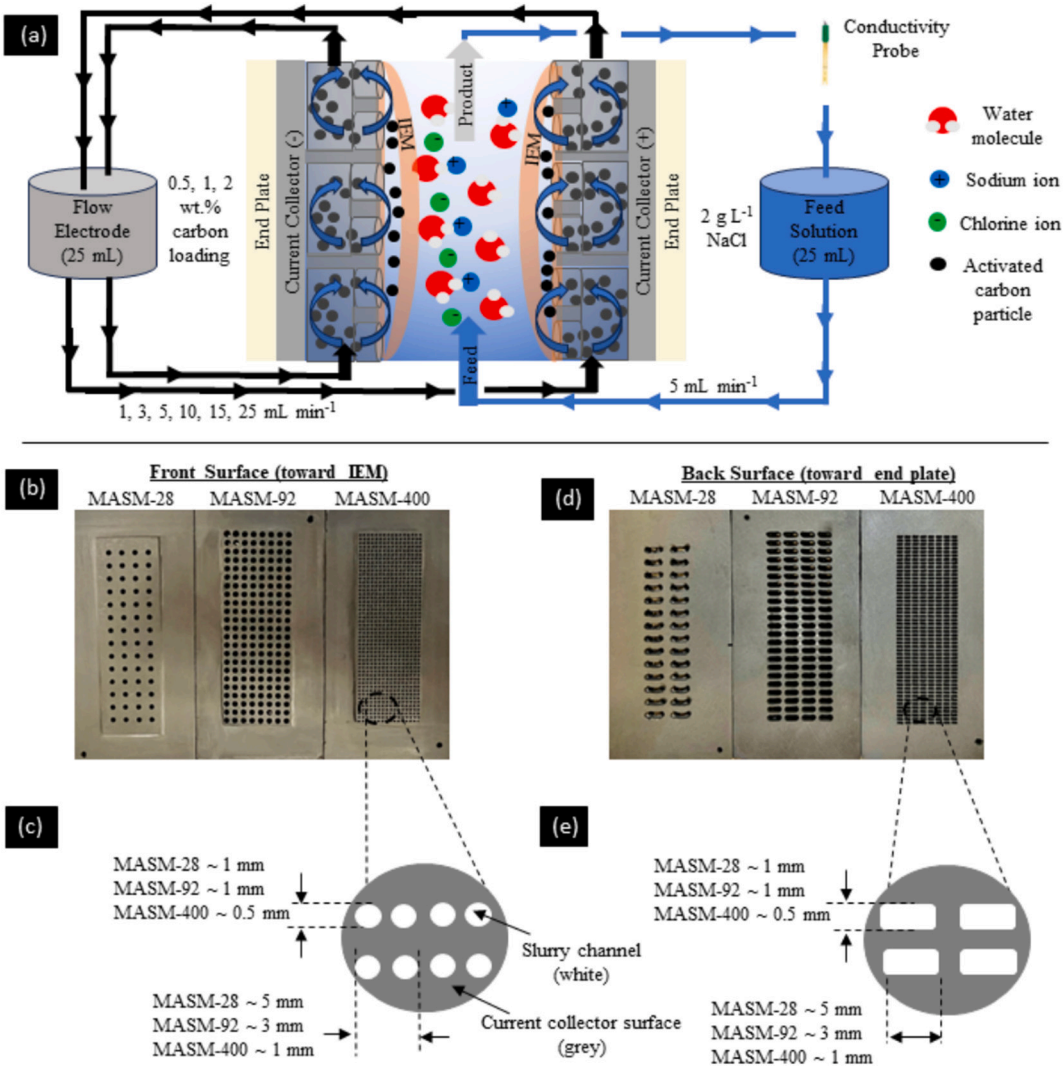

Fig. 2. A schematic of the FCDI system used in SCC mode is shown in (a), while the static mixers machined from graphite plates are shown in (b) and (d). Dimensions of the plates are outlined in c & e, where holes were drilled through the front surface (c) and slots machined into the back surface (e) using a desktop CNC machine.

Table 1
Experimental parameters.

Flow field	Channel length (cm)	IEM-CC contact area[1] (cm^2)	Flow field dimensions (cm)	Carbon loading (wt%)	Flow rate (mL min^{-1})
OC-0	–	18.75	7.5 × 2.5 (zero-gap flow fields)	0.5, 1, 2	1, 3, 5, 10, 15, 25
MASM-28	0.7	16.4			
MASM-92	0.55	13.0			
MASM-400	0.25	12.5			
OC-75	–	–	7.5 × 2.5 × 0.075		

[1] IEM-CC contact area is defined as the surface area between the ion-exchange membrane and the current collector for zero-gap flow fields.

were unknown. Therefore, to investigate the relation between channel dimensions, number of channels, electrochemical performance, and hydrodynamic losses, the MASM-x geometry was varied according to Table 1.

Lastly, the current collector surface area in contact with the IEM is an important feature as a greater surface area increases the rate of particle-current collector interactions and therefore improves the probability of ion adsorption. However, too large of an IEM-CC surface area will create direct pathways for the carbon particles to follow and immediately leave the cell. Therefore, a balance between the channel dimensions and IEM-CC contact surface area must be met.

2.3. Electrochemical testing

FCDI tests were conducted in short-circuited closed-cycle mode (SCC) with a total slurry volume of 25 mL while 25 mL of feed water solution (2 g L^{-1} NaCl) was circulated through the FCDI cell via peristaltic pumps (Cole Palmer Masterflex). The feed water solution was maintained at a constant flow rate of 5 mL min^{-1}, while the slurry flow rates of 1, 3, 5, 10, 15, and 25 mL min^{-1} were applied. Pressure and conductivity values were recorded with flow-through sensors (Atlas Scientific), while electrochemical data was collected using a Biologic VSP potentiostat. Both chronoamperometry and long adsorption tests were conducted at 1.2 V using a two-electrode setup for 15 min and 90 min, respectively. Lastly, EIS tests scanned from 200 kHz to 0.5 mHz frequency range with a 50-mV amplitude and were conducted under optimal flow configurations.

The effects of the flow field geometry on the desalination performance were investigated using the following equations:

$$\text{ASRR}\ \left(\text{ug cm}^{-2}\ \text{s}^{-1}\right) = \frac{\left(C_f - C_d\right)q}{A_{eff}} \quad (1)$$

$$\text{Electrical Energy Consumption}\ \left(\text{kJ mol}^{-1}\right) = \frac{M \cdot U \int_0^t I dt}{\left(C_f - C_d\right) \cdot V \cdot 10^{-3}} \quad (2)$$

$$\text{Pumping energy consumption}\ \left(\text{kJ mol}^{-1}\right) = \frac{M \cdot 2 \cdot \Delta p \cdot q \cdot t}{\left(C_f - C_d\right) \cdot V \cdot 10^{-3}} \quad (3)$$

$$\text{Total energy consumption}\ \left(\text{kJ mol}^{-1}\right) = \frac{M \cdot U \int_0^t I dt + M \cdot 2 \cdot \Delta p \cdot q \cdot t}{\left(C_f - C_d\right) \cdot V \cdot 10^{-3}} \quad (4)$$

where C_f and C_d are the initial salt and final salt concentrations (μg L^{-1}) of the water stream, q is the volume flow rate (L s^{-1}) of the water stream, V is the volume of feed solution (L), A_{eff} is the effective surface area (cm^2), i.e., the area of contact between the slurry and IEM, M is the molar mass of NaCl, U is the applied voltage (V) of 1.2 V vs. open-circuit voltage (OCV), and Δp is the average pressure drop (Pa) of the slurry channels.

3. Results and discussion

3.1. Indirect methods for assessing the membrane–assisted mechanism

The proposed membrane-assisted mechanism outlined in Fig. 3 (see steps 1–8) utilizes the cyclic displacement of the IEM to sufficiently mix the AC particles within the flow field while simultaneously minimizing charge transport distances. Since it is difficult to directly observe the membrane-assisted mechanism while conducting desalination experiments, several indirect methods were chosen.

First, flow dampener attachments were used to lessen the pressure fluctuations from the peristaltic pumps, as seen in Fig. 3g. The dampened MASM-92 with an ASRR of 1.833 μg cm^{-2} s^{-1} were nearly identical to OC-0 with an ASRR of 1.717 μg cm^{-2} s^{-1} (Fig. 3h), while the undampened MASM-92 revealed a much higher ASRR of 4.416 μg cm^{-2} s^{-1}. The constant pressure of the dampened MASM-92 (Fig. 3g) indicated that by dampening the flow, the membrane remained bulged away from the current collector in a fixed parabolic shape. The bulged membrane likely caused the particles to travel along the surface of the

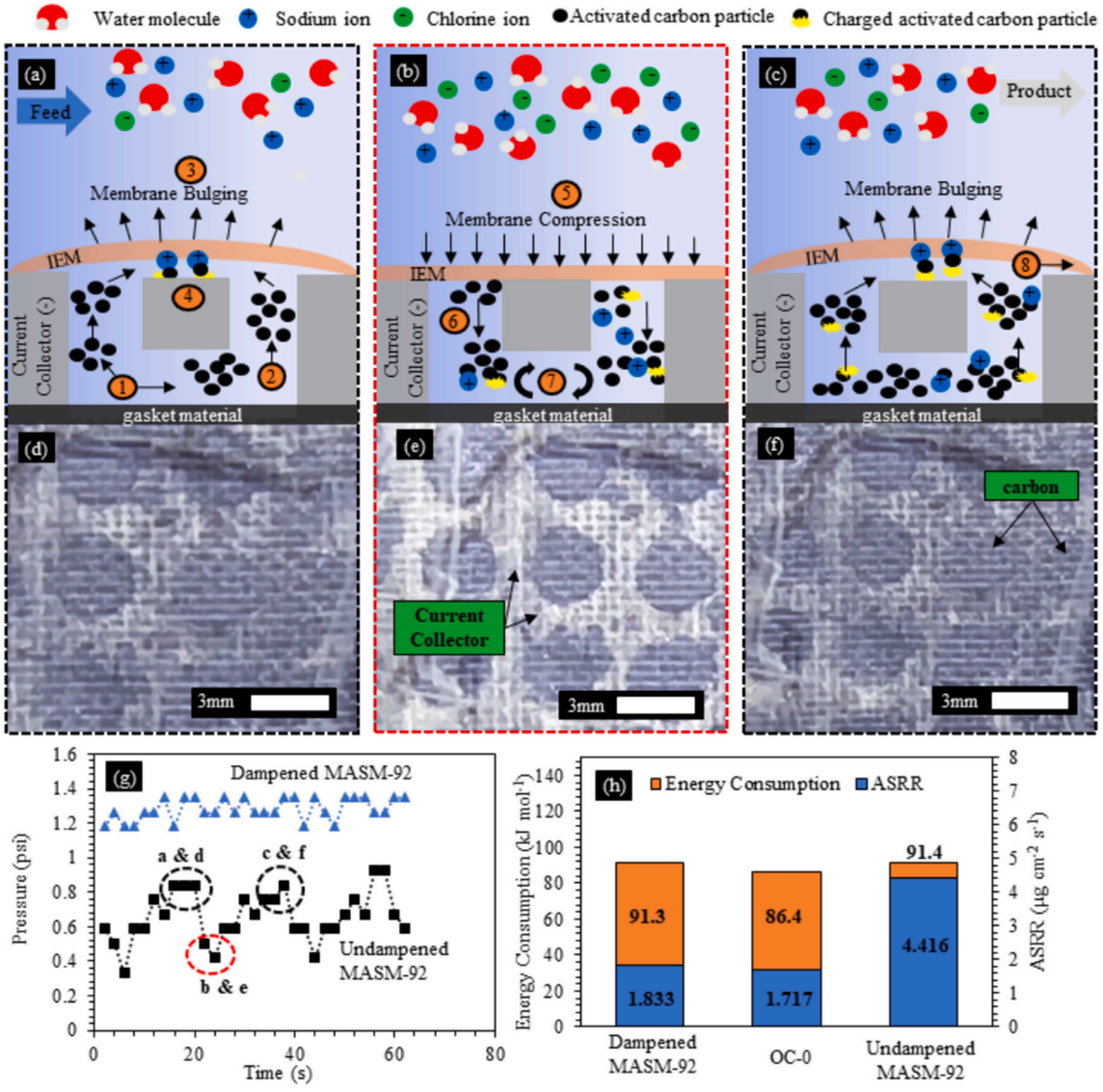

Fig. 3. Illustrations of a single channel within the MASM flow field (a–c) and their corresponding images (d–f) are shown for one pressure cycle. The membrane-assisted mechanism is outlined by the following: 1) slurry inlet, 2) flow toward the membrane, 3) membrane bulging at pressure peak, 4) ion adsorption, 5) membrane compression at pressure valley, 6) flow toward channel, 7) particle mixing and 8) membrane bulging followed by particle flow toward the outlet. Pressure fluctuations (g) and desalination performance (h) of the dampened MASM-92, undampened MASM-92 and OC-0 are compared.

MASM-92 current collector and helped them perform in a similar way to an open channel design. These results ultimately showed that pressure fluctuation was a necessary feature to improve the electrochemical performance. Additional tests were performed while flowing the slurry at 15 mL min^{-1} with no applied voltage to observe the effect of the pressure fluctuations on the carbon particles themselves, discussed in Section 3.3.1.

Another method chosen to assess the membrane-assisted mechanism was the direct observation of the fluid flow while pumping the slurry at various flow rates. This was done by assembling a half-cell with a transparent acrylic plate on the outer surface. Images of the MASM-92 at 15 mL min^{-1} flow rate were shown for one pressure cycle in Fig. 3d–f. The carbon particles that were drawn toward the IEM at pressure peaks (Fig. 3d, f) appeared to obscure the current collector surface, while the surface was clearly visible at lower pressures (Fig. 3e) as the carbon particles were forced into the machined channels. The membrane-assisted mechanism was evident both in the anion-exchange membrane (AEM) and cation-exchange membrane (CEM) as a rhythmic mixing of particles was observed.

Lastly, the OC-0 flow field was chosen as a reference flow field since its charge transfer distances were identical to MASM-x without the addition of channels. Therefore, any performance improvements between the OC-0 and MASMs were credited to the static mixer geometry.

3.2. Electrochemical performance

In an FCDI system, the reactions ideally take place at the interface between the ion-exchange membrane and the current collector. At this interface, ions travel from the feed stream, through the IEM, and onto the porous carbon surface. However, in the FCDI literature, little consideration has been given to minimizing the distance between the current collector and IEM. This is mainly due to the nature of the studied flow field designs that rely upon the percolation networks to achieve sufficient charge transfer. Instead, the MASM design promotes particle–current collector interactions near the IEM interface, where the distance required for ions to travel from the feed stream and onto a particle surface is minimized. To better assess the merits of this behavior, the electrochemical performances of the studied MASM-x designs were characterized using chronoamperometry and electrochemical impedance spectroscopy.

3.2.1. Chronoamperometry (CA) results

CA tests were conducted over a 15-min period with 25 mL of 2 g L^{-1} of NaCl feed solution at a 5 mL min^{-1} flow rate and an equal volume of slurry at flow rates of 1, 3, 5, 10, 15, and 25 mL min^{-1}. Overall results (Fig. 4) at 2 wt% AC indicated a significant improvement in current response with increasing flow rate for all flow fields. Similar trends were observed at 0.5 wt% and 1 wt% AC (Figs. S1, S2). Meanwhile, zero-gap

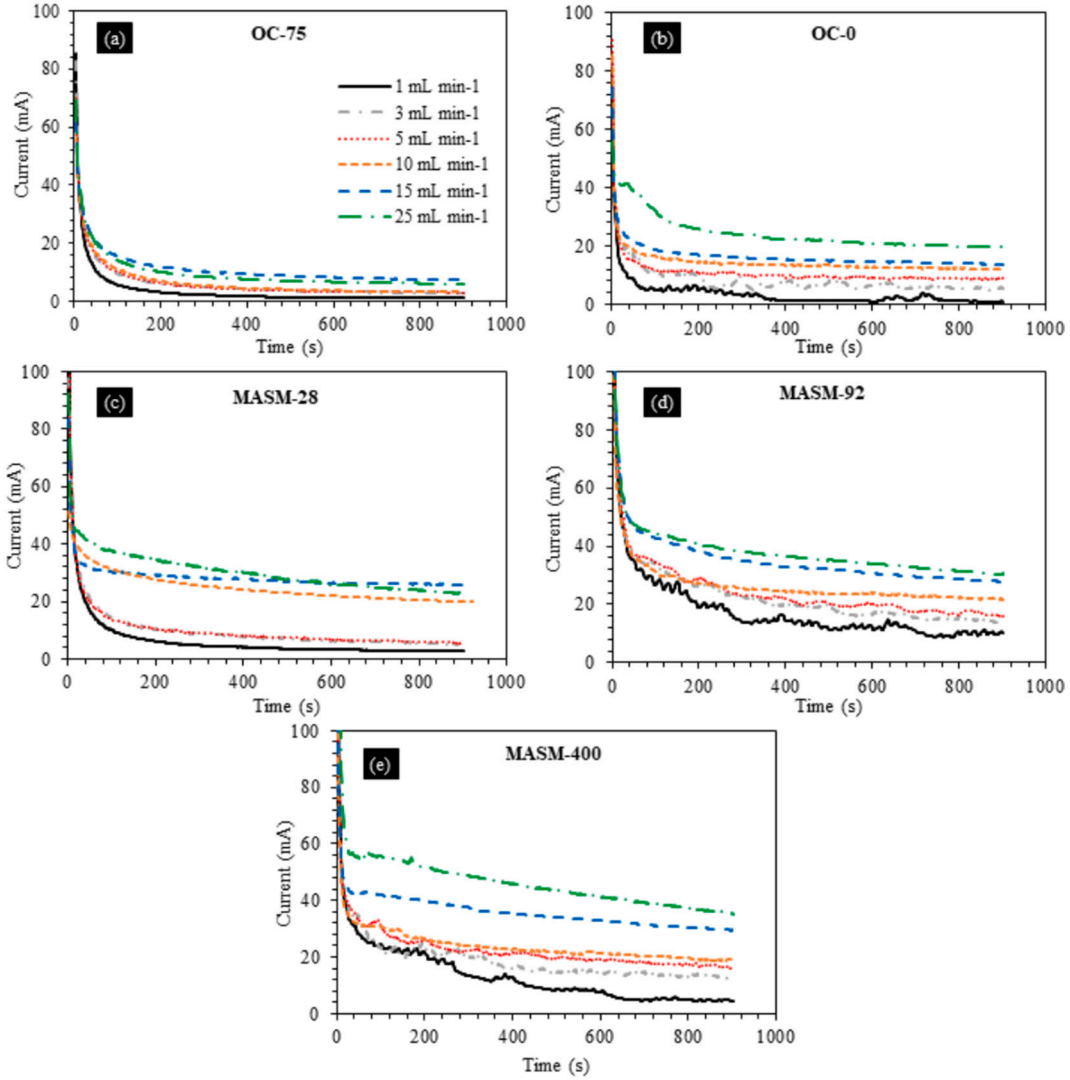

Fig. 4. The current response is shown for each flow field at 2 wt% carbon loading and flow rates of 1, 3, 5, 10, 15 and 25 mL min^{-1}.

flow fields (OC-0, MASM-x) showed much higher current response compared to the traditional flow field (OC-75) design and was likely a result of the reduced charge transfer distances between the carbon particles and current collector.

In comparing both open channel flow fields, the steady-state current response at 25 mL min^{-1} increased from 6 mA to 19 mA for the OC-75 and OC-0 design, respectively. Similar trends were observed across all flow rates, where the OC-0 flow field showed approximately a 3× increase in current density. In comparing OC-0 with MASM-x designs, the MASM-x designs displayed improved current response for all flow rates and particularly outperformed OC-0 at lower flow rates of 1–5 mL min^{-1}. At higher flow rates of 15 mL min^{-1} and 25 mL min^{-1}, there was a noticeable increase in current response for each MASM-x design, where MASM-92 and MASM-400 showed the highest steady-state current response at 25 mL min^{-1} of 30 mA and 35 mA, respectively. Interestingly, at flow rates of 15 mL min^{-1} and 25 mL min^{-1}, the current values appeared to converge after some time, indicating that 25 mL min^{-1} may be a maximum flow rate for the MASM-x geometries. From the CA data, it was clear that the reduction in charge transport distances of the zero-gap flow fields greatly increased the current density of the system. Additionally, the MASM geometry further improved the current response by increasing the rate of particle mixing and inducing chaotic flow behavior among the AC particles. This increased particle mixing has been shown to increase the current response of flowable electrodes in other static mixer designs [20]. To further analyze the effect of the MASM geometry on the conductivity of the system EIS was performed at a constant flow rate of 15 mL min^{-1}.

3.2.2. *Electrochemical impedance spectroscopy (EIS)*

EIS was used to relate the contact resistance and the current response to the flow field geometry. The high-frequency response of the system, due to the presence of contact resistance between the particles and the current collector, can be viewed along the intersection of the x-axis [30]. The MASM-28 design showed the least contact resistance of 2.95 Ω, followed by 3.26 Ω (MASM-92), 3.95 Ω (MASM-400), 4.92 Ω (OC-0), and 7.44 Ω (OC-75) (see Fig. 5).

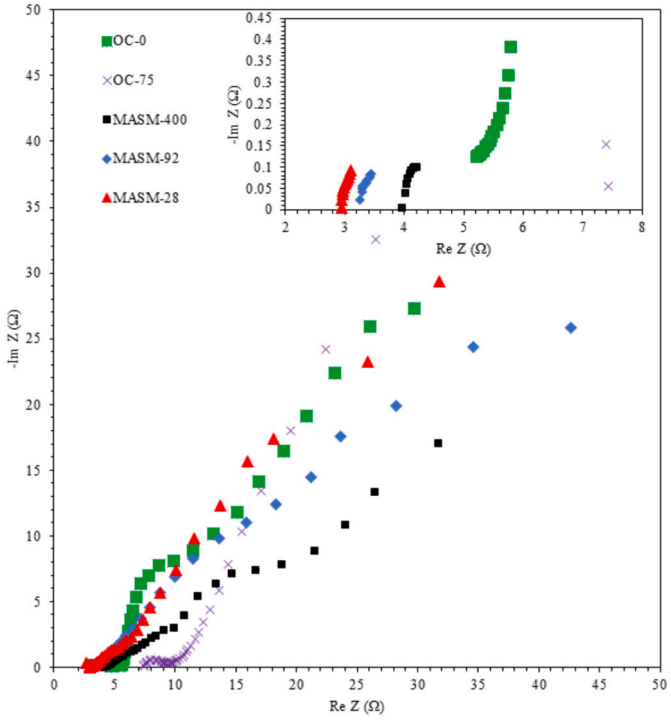

Fig. 5. Nyquist plot of each flow field under the optimized conditions, evaluated at 200 kHz to 0.5 mHz with amplitudes of 50 mV.

The lower ohmic resistances observed for MASM designs and OC-0 compared to OC-75 indicated the existence of reduced contact resistance among the static mixer geometry and can be attributed to the decreased charge transfer distance as the IEM was compressed directly onto the CC surface [29]. Given that the high-frequency response is solely accommodated by particle–current collector contact, a flow field with a high current collector surface area is expected to have a lower resistance at high frequencies. In the MASM-x designs, there were two surface areas differentiated by their charge transport distances. As previously mentioned, the IEM-CC contact surface area approaches a zero-gap charge transport distance, while the contact surface areas of the channel walls have large charge transport distances of 0.5–5 mm. As the number of channels is increased from 28 channels (MASM-28) to 400 channels (MASM-400), the current collector contact surface area of the channels increases from 18.5 cm^2 to 105 cm^2. However, the increased channel surface area of 105 cm^2 did not lead to improved impedance values. These results suggest that the channel walls have little impact on the impedance as the charge transport distances were too large for low carbon loading suspensions. Instead, EIS results showed that the surface area along the IEM-CC interface had a greater effect on contact surface resistance compared to the surface area along the channel walls. As seen in Table 1, the increasing IEM-CC contact surface area (i.e., $Area_{MASM-28} > Area_{MASM-92} > Area_{MASM-400}$) corresponds to lower resistances.

In EIS analysis, as the frequency decreases, particle mixing becomes more dominant and is represented by the Nyquist plot's semi-circle radius. Higher rates of particle interactions have been shown to increase the current response of the system, which is also referenced by other studies [30,31] as “convective current”. Therefore, the radius of the semi-circle can be directly related to the quality of mixing within the flow field. In Fig. 4, the radius of the semi-circle for OC-75 and MASM-28 had large impedance values, while MASM-92 and MASM-400 showed smaller radii of curvature. It is reasonable to assume that the MASM-92 and MASM-400 mixed the carbon particles more thoroughly. The relation between convective current and desalination performance was further explored by comparing ASRR vs. flow rate and discussed in Section 3.3.2.

3.3. *Desalination performance*

Desalination performance is typically quantified by the rate of ion adsorption per unit area (ASRR) and the total energy consumption per mole of adsorbed ions (kJ mol^{-1}). In FCDI systems, the desalination performance is largely dependent upon the electrical conductivity and advection of active material. As discussed in Section 3.2, the MASM design showed improved contact resistances compared to the open channel configuration and improved current response with increasing flow rates. In this section, the desalination performance was investigated with respect to each MASM-x geometry under static and dynamic flow conditions. The best performing flow configuration was then evaluated according to the total energy consumption by calculating both electrical and pumping energy requirements. Lastly, the best performing flow configuration was used for long-term desalination tests.

3.3.1. *Effect of static mixer geometry on desalination performance*

In this section, the MASM-x geometry was investigated while applying a constant voltage of 1.2 V at 15 mL min^{-1} flow rate, shown in Fig. 6a, b. Additional tests were conducted (Fig. 6c, d) for each MASM-x flow field to observe any effects of electrodialysis, physiochemical changes among the AC particles and ion adsorption within the flow channels.

According to Fig. 6a, b, the MASM-x designs removed 36–40 % of the salt, while OC-0 and OC-75 removed 20 % and 12 % of the salt, respectively. The improvement in desalination performance and rapid charge transfer of the MASM-x designs were attributed to enhanced particle–current collector interactions and induced particle mixing compared to the open channel designs. The small gap formed at the IEM-

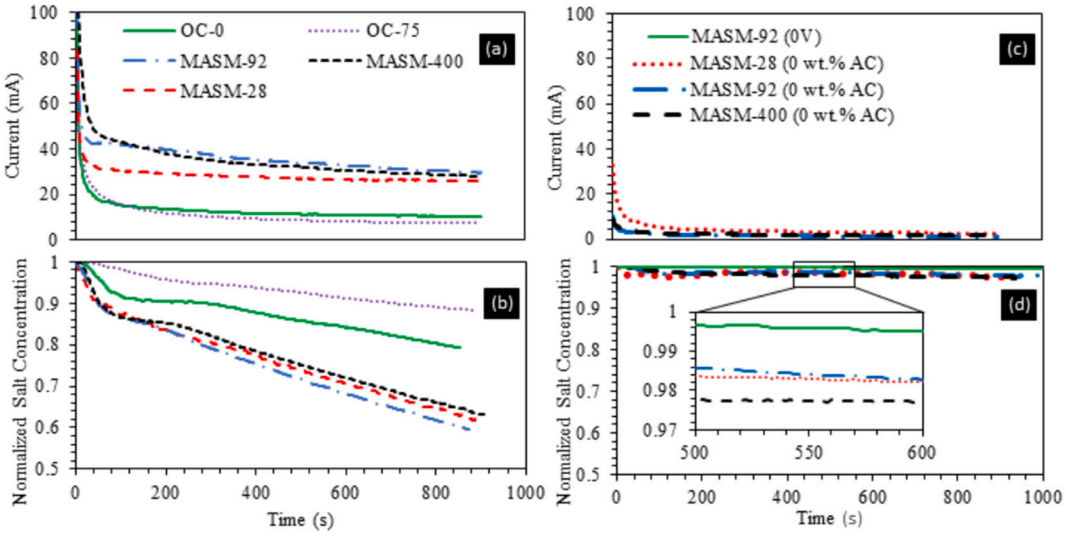

Fig. 6. The current response (a) and effluent salt concentrations (b) are shown for each flow field operating at 15 mL min^{-1} slurry flow rate. Additional tests (c, d) were performed to eliminate possible electrodialysis and physiochemical adsorption contributions. The IEM-CC contact areas for each flow field are provided: OC-0 (18.75 cm^2), MASM-28 (16.4 cm^2), MASM-92 (13.0 cm^2), MASM-400 (12.5 cm^2) and OC-75 (0 cm^2).

CC interface significantly reduced the salt ion diffusion distances and likely allowed salt adsorption to occur more easily. The decreased charge transport distances also increased the kinetic performance of the MASM-x designs, resulting in over 200 % and 350 % increase in salt removal within the first 2 min of testing compared to OC-0 and OC-75, respectively.

While the reduced charge transport distance was likely the greatest contributor to the improved desalination performance of the MASM-x designs, the IEM-CC contact surface area and the channel dimensions seem to have also influenced the desalination performance. As the membrane bulged, AC particles were drawn toward the IEM and contacted the CC at the IEM-CC interface. The IEM-CC contact surface area was considered an important metric as it determines the number of particle-current collector interactions, where a greater surface area (of the current collector) increases the likelihood of the enhanced charge transfer. Accordingly, MASM-92 with an IEM-CC contact surface area of 13 cm^2 was observed to remove 4 % more salt compared to the MASM-400 with an IEM-CC contact surface area of 12.5 cm^2. However, MASM-28 had a larger IEM-CC contact surface area (16.4 cm^2) than MASM-92, yet MASM-28 did not have improved salt adsorption over the MASM-92. This discrepancy may be attributed to the quality of mixing within the flow field. Due to the low number of channels within the MASM-28 flow field, the carbon particles likely found a direct path to the outlet and reduced the residence times of the carbon particles within the flow field, similar to the flow behavior of the OC-0 flow field.

Another important consideration that can potentially influence the desalination performance of the static mixer designs is electrodialysis (ED). ED was investigated by conducting CA tests without activated carbon or conductive additive present in the flowable electrode (Fig. 6c, d). The current response and desalination performance of the 0 wt% AC were found to be remarkably low, indicating that ED contributed little to the electrochemical performance of the static mixer geometry. CA tests were also conducted under static conditions while the IEMs remained compressed on the current collector surface to determine the importance of channel dimensions on the ion adsorption process. While the salt concentration was initially reduced, the amount of salt removed did not drop below 5 %. This reduced current response and desalination performance showed that the low carbon loading slurry was below the percolation threshold, and the channel dimensions were too large to have an appreciable impact on the conductivity while under static configuration.

Lastly, CA tests were also conducted under flow conditions at 15 mL min^{-1} slurry flow rate with no applied voltage to investigate possible salt adsorption due to physiochemical changes among the carbon particles. There was a small drop in salt concentration of <0.5 %, shown in Fig. 6c, d, which was likely due to the higher salt concentration of the feed stream diffusing into the slurry channels over the 15-min test. Given the small change in feed solution concentration, it is likely the salt adsorption was not aided by the flow conditions of the carbon particles alone.

3.3.2. *Effect of flow rate on ASRR*

In Fig. 7, the ASRR was plotted against the flow rate for each flow field at carbon loadings of 0.5, 1 and 2 wt%. The OC-75 flow field (Fig. 7a), which represents a traditional open channel flow field, showed a modest increase in ASRR with increasing flow rate and had a maximum ASRR of 1.6 μg cm^{-2} s^{-1} at 25 mL min^{-1} and 2 wt% AC. The OC-0 flow field (Fig. 7b) appeared to have a higher ASRR compared to the OC-75 design at all flow rates and carbon loadings since the charge transfer distances were significantly reduced. There was a noticeable improvement in ASRR for the OC-0 flow field at 2 wt% AC and 5 mL min^{-1}, but the ASRR quickly plateaued after a 10 mL min^{-1} flow rate and reached a maximum ASRR of 2.5 μg cm^{-2} s^{-1} at 2 wt% AC and 25 mL min^{-1}.

Among the MASM flow fields, the MASM-28 performed similar to the OC-0 at 0.5 wt% and 1 wt% AC and slightly improved in desalination performance at 2 wt% AC. However, the desalination performance of MASM-28 began to drop at 25 mL min^{-1}. The low number of channels within the MASM-28 flow field likely caused particles to follow a direct path from inlet to outlet, as too few channels were available to disrupt the flow of the particles at higher flow rates.

The MASM-92 (Fig. 7d) and MASM-400 (Fig. 7e) showed exceptional performance, with maximum ASRRs of 5.5 μg cm^{-2} s^{-1} and 4.83 μg cm^{-2} s^{-1}, respectively. In Fig. S3a–c, the percentage increase in ASRR compared to the OC-0 reference flow field was plotted against the flow rate for each carbon loading. The MASM-92 and MASM-400 showed a 100 % increase in ASRR at 15 mL min^{-1} for both 0.5 wt% and 1 wt% AC. At low flow rates, the percent increase in ASRR jumped to over 300 % at 3 mL min^{-1} and 5 mL min^{-1} with 0.5 wt% AC.

In Fig. 7d, the MASM-92 displayed a large difference in the ASRR for 0.5 wt% AC when compared to 1 and 2 wt% AC, suggesting that there was a minimal carbon loading necessary to improve conductivity within the MASM-92 geometry. Similarly, the MASM-400 displayed a large difference in ASRR between 2 wt% carbon loading and 0.5 and 1 wt%

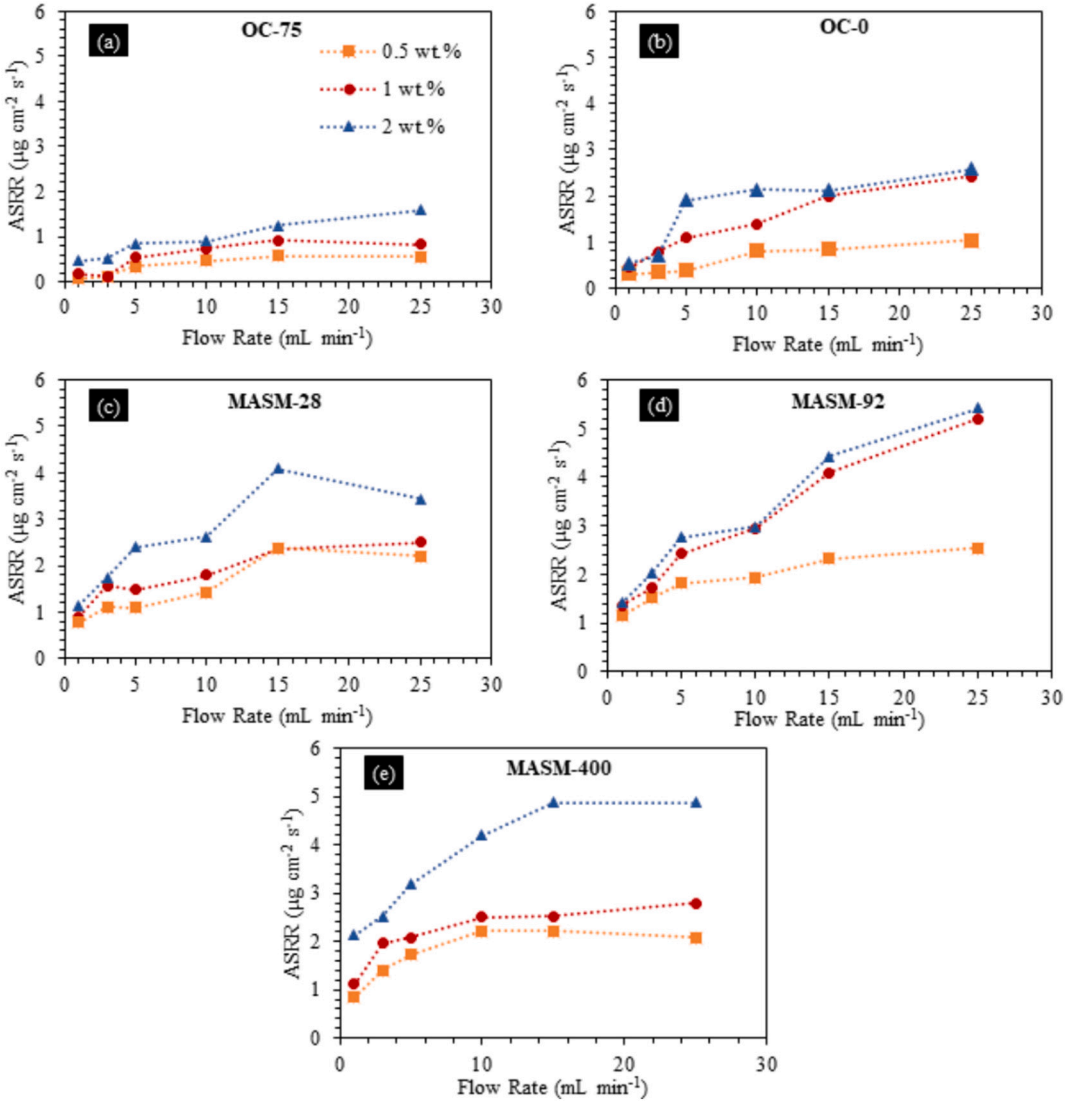

Fig. 7. The ASRR vs. flow rate is shown for each flow field across carbon loadings of 0.5, 1 and 2 wt% and flow rates of 1, 3, 5, 10, 15 and 25 mL min^{-1}.

carbon loading, indicating that the MASM-400 needed higher carbon loading to achieve similar ASRR as compared to the MASM-92. The highest ASRRs were observed for the MASM-92 and MASM-400 at 15 and 25 mL min^{-1}; however, further inspection of electrical energy consumption and pumping energy requirements were needed to determine the best performing flow configuration.

3.3.3. *Kinetic analysis of desalination performance*

The MASM-x designs revealed exceptional kinetic performance in the first 100 s of desalination testing which is shown for 3 mL min^{-1} (Fig. 8a) and 15 mL min^{-1} (Fig. 8b) slurry flow rate. During the first 100 s (kinetic regime), the feed solution conductivity sensor measured approximately 10–13 wt% of salt removal for each MASM-x flow field, regardless of the flow rate. The sharp decrease in feed concentration in the kinetic regime was due to the instantaneous adsorption of ions onto the fresh uncharged carbon particles interacting with the current collector. The quality of mixing and IEM-CC contact surface area outlined in the EIS results also influenced the rate of ion adsorption during this time; however, it is clear that all MASM-x designs showed a sharp decrease in salt removal in the kinetic regime for both low (3 mL min^{-1}) and high (15 mL min^{-1}) flow rates. Given the feed solution was pumped at a constant flow rate of 5 mL min^{-1}, the conductivity sensor had a delayed response as fresh feed solution was pumped into the middle chamber. Unsurprisingly, this sharp increase in salt removal did not remain constant. After 100 s, the salt removal was no longer dominated by the kinetic response of the system but was instead dominated by the advection of carbon particles within the flow field. At 3 mL min^{-1}, the measured salt concentration began to rise as new feed solution continued to enter the middle chamber at the initial salt concentration. This decreased salt removal showed that the advection of the carbon particles was the limiting factor and a higher slurry flow rate would be needed to improve the desalination performance. At 15 mL min^{-1}, the salt concentration did not rise but instead decreased, albeit at a slower salt removal rate. This decrease in salt concentration indicated that the advection response of the system improved with increasing flow rate but was still a limiting factor in the salt removal process. However, increasing the flow rate of the slurry was accompanied by increased hydrodynamic losses and increased pumping energy requirements.

3.3.4. *Pumping and electrical energy consumption*

Pumping energy consumption is one of the most critical design aspects of a flowable system and is considered an internal loss which should be minimized to reduce the required pumping cost [25]. In the MASM design, pressure was generated due to the compression of the IEM against the current collector surface. This level of compression was maintained constant across all MASM designs; however the channel size

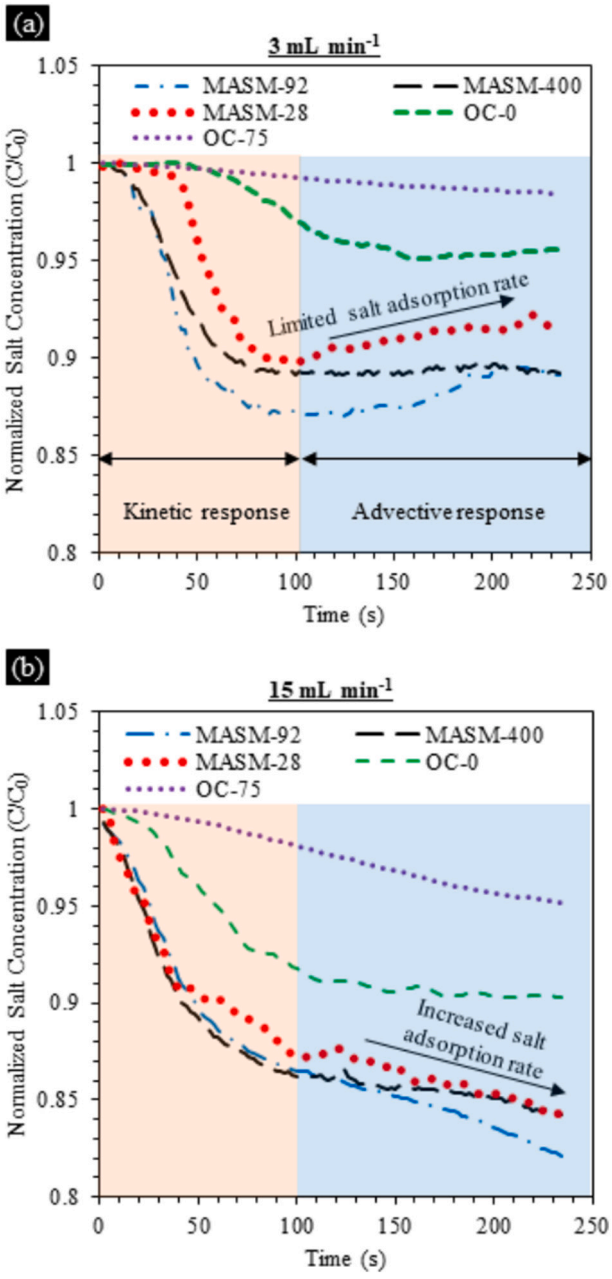

Fig. 8. The charge transfer kinetics of each flow field is characterized by analyzing the salt concentration during the first 250 s of desalination at flow rates of 3 mL min^{-1} (a) and 15 mL min^{-1}.

and number of channels did vary between MASM-28, 92 and 400. Pumping energy consumption (kJ mol^{-1}) among MASM-x (2 wt%AC), OC-0 (2 wt%AC) and OC-75 (10 wt% AC) designs are shown in Fig. 9. At flow rates of 1–5 mL min^{-1}, each flow field consumed <5 kJ mol^{-1}, except for the OC-0 flow field. This was due to the high pressure drop of the OC-0 design, shown in Fig. S4, combined with the relatively low desalination performance. At 10 mL min^{-1} and 15 mL min^{-1} flow rates, the MASM-92 and MASM-400 flow fields maintained the lowest pumping energy consumption values. However, at 25 mL min^{-1} flow rate, the MASM-92 and MASM-400 performed the best in terms of pumping energy consumption, with values of 16.5 kJ mol^{-1} and 18.4 kJ mol^{-1}, respectively.

Upon analyzing the pressure drop of each flow field, the MASM-400 configuration consistently showed the highest pressure drop across all flow rates. These high pumping requirements were likely a result of the

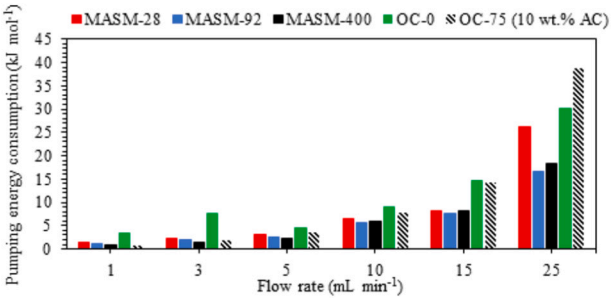

Fig. 9. Pumping energy consumption for all zero-gap flow fields at 2 wt% AC and OC-75 at 10 wt% AC.

high number of channels and frictional losses occurring at the walls of the channels. Similar behavior was also observed in the MASM-92 and MASM-28 designs, where MASM-92 (i.e., more obstructions) consistently displayed higher pressure drop as compared to MASM-28 (i.e., fewer obstructions) for all carbon loadings and flow rates. At lower flow rates of 1–5 mL min^{-1}, the MASM-28 showed lower pressure drop values. The geometry of the MASM-28 was favorable toward lower flow rate configurations as the channels machined into the current collector were larger than MASM-92 and MASM-400; however, above 5 mL min^{-1} flow rate the pumping energy consumption of MASM-28 became equivalent to MASM-92 and OC-0.

A traditional flow field at 10 wt% AC was also shown as a reference to better evaluate the zero-gap flow fields pumping energy requirements. The open channel configuration displayed lower pressure drop values compared to all zero-gap flow fields as there was no compressive force acting against the slurry upon entering the cell. However, the pumping energy consumption of the OC-75 flow field at 10 wt% was similar to OC-0 at 2 wt% AC and 15 mL min^{-1} of 14.14 kJ mol^{-1}. Additionally, the OC-75 at 10 wt% revealed the highest pumping energy consumption of 38.69 kJ mol^{-1} out of all the flow fields in this work. Desalination and electrical energy consumption from other reports were shown in Table 2 for comparison against 10 wt% AC slurries and this work.

To evaluate the best performing flow configuration, both pumping energy consumption and electrical energy consumption were taken into account, where the electrical energy consumption vs. ASRR is shown in Fig. 10. The flow fields demonstrating the highest ASRR were considered among the best performing flow configurations and analyzed by their total energy consumption values. The MASM-92 and MASM-400 showed the highest ASRR values at 15 mL min^{-1} and 25 mL min^{-1}. At 15 mL min^{-1}, the MASM-92 and MASM-400 flow fields revealed similar electrical energy consumption values of 91.3 kJ mol^{-1} and 94.3 kJ mol^{-1}, respectively; however, the MASM-92 and MASM-400 revealed a total energy consumption of 98.95 kJ mol^{-1} and 102.35 kJ mol^{-1} at 15 mL min^{-1} flow rates respectively. At 25 mL min^{-1} flow rates, the MASM-92 and MASM-400 showed total energy consumption values of 112.97 kJ mol^{-1} and 105 kJ mol^{-1}. Considering the lower total energy consumption values of the MASM-92 at 15 mL min^{-1} while maintaining a high ASRR of 4.423 μg cm^{-2} s^{-1}, the MASM-92 flow field was considered the best-performing case among the tested flow configurations and was used for the long-term desalination tests over a 90-min period.

3.3.5. *Long desalination tests*

In order to demonstrate the long-term performance of the MASM design, single-step chronoamperometry tests were conducted over a 90-min period under SCC mode. SCC mode is considered a more efficient flow configuration for FCDI since the previously captured ions are released upon contact with oppositely charged particles or current collector [36]. Once released into the electrolyte, the carbon particles are considered replenished and therefore avoid ion-saturation within the porous structure. In the MASM flow configuration, the carbon particles

Table 2
Comparison of recent FCDI reports using ASRR and energy consumption as performance metrics.

Electrode material	Active material loading (wt%)	Initial salt concentration (ppm)	Applied current/ voltage	ASRR (μg cm^{-2} s^{-1})	Energy consumption (kJ mol^{-1})	Year published [reference]
DARCO + Norit AC	10	1000	0.909 mA cm^{-2}	1.12	35.79	2020 [32]
			1.818 mA cm^{-2}	2.30	162.61	
AC + CB	5.72	10,000		1.83	–	2019 [33]
AC + CB + ferri-/ferrocyanide	10	9000	0.47 mA cm^{-2}	0.16	40.95	2020 [34]
			2.38 mA cm^{-2}	1.33	98.07	
			4.28 mA cm^{-2}	2.7	160.0	
ZIF-8 nanoporous carbon polyhedron	10	3000	0.6 mA cm^{-2}	0.349	–	2022 [35]
AC	12.5	3500	1.2 V	3.204	–	2022 [28]
AC + CB	0.5	2000	1.2 V	1.760	43.7	This work
	1			4.089	97.8	
	2			4.423	91.3	

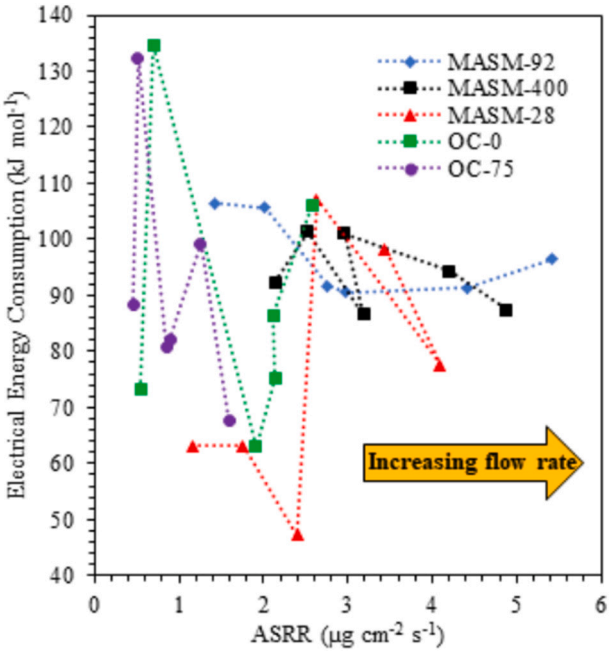

Fig. 10. Electrical energy consumption vs. ASRR is shown for each flow field at 2 wt% AC.

were more readily mixed within the flow field and therefore short-circuited more often leading to higher overall salt adsorption. Demonstration of the long-term desalination performance and short-circuiting ability of the MASM was shown in Fig. 11, where a feed water to slurry volume ratio of 5:1 was chosen. At a 1:1 ratio of feed water to carbon suspension volume, the MASM-92 was capable of desalinating the entire feed stream within the first 40 min of testing. Therefore, the feed water to slurry volume ratio was increased to a 5:1 ratio to utilize the active material fully. In commercial applications, having a smaller flowable electrode-to-feed water volume ratio is critical for maintaining infrastructure costs at lower margins (i.e., reservoir size, pipe diameter, etc.) and minimizing the hydrodynamic losses. As shown in Fig. 11, the MASM-92 configuration removed 23 % of the salt from the 125 mL feed water solution, while OC-0 and OC-75 were only able to remove 7.5 % and 5.7 %, respectively. The results showed that carbon mass in the slurry electrodes was effectively utilized since no channel clogging during the experimentation and particle sedimentation after disassembling the cell were observed.

4. Conclusion

In this study, a new type of flow field (referred to as a membrane-assisted static mixer -MASM) was proposed that showed significantly improved desalination performance and carbon utilization in a lab-scale FCDI device. MASMs improved charge transfer kinetics by compressing the IEMs against the surface of the flow field and reduced the charge transfer distance to a small gap formed by the membrane's relative motion during pressure fluctuations. The channels machined into the back of the flow field were observed to increase the residence time of the

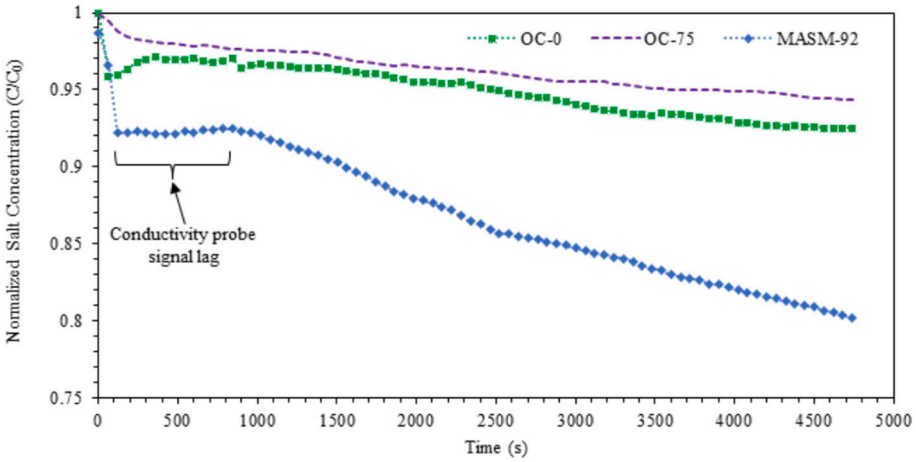

Fig. 11. Desalination tests were conducted at 5:1 ratios of feed water to slurry volume for each OC-0, OC-75 and MASM-92 flow configuration under best performing conditions (2 wt% AC and 15 mL min^{-1} flow rate).

carbon particles and enable mixing of the particles during pressure fluctuations.

Three separate MASM geometries were studied by varying the slurry electrode flow rate (1–25 mL min^{-1}) and activated carbon loadings (0.5–2 wt% AC). Chronoamperometry and EIS results revealed that the majority of the charge transfer occurred at the IEM-CC interface rather than within the channels of the flow field. The channel configuration (i.e., number of channels and dimensions) was observed to impact the convective current and overall desalination performance as the quality of mixing increased with an increasing number of channels. An optimum balance of IEM-CC contact area and channel configuration was met with the best-performing flow configuration (MASM-92, 2 wt% AC @ 15 mL min^{-1}) and showed a high ASRR of 4.423 μg cm^{-2} s^{-1} with an energy consumption of 98.95 kJ mol^{-1}. These results were compared to both reference flow fields, which revealed over a 250 % increase in ASRR during 15-min desalination tests and a three-fold increase in salt removal capacity over a 90-min test when compared to the open channel configuration (OC-75). The MASM designs particularly outperformed traditional open channel flow fields at low flow rates (1–5 mL min^{-1}) and showed nearly a 400 % increase in ASRR at 5 mL min^{-1}.

Further studies are needed to optimize the MASM geometry by altering the channel depth and orientation with respect to the outlet (i.e., diagonal, vertical, etc.). These alterations may help achieve more uniform flow field designs by avoiding “dead zones” where particles get trapped and decrease carbon utilization. Alternatively, coupling redox-active species and/or high aspect ratio nanomaterials (i.e., carbon nanotubes, graphene) with the MASM design may also offer synergistic effects that could further improve desalination performance of the low carbon loading FCDI systems.

Supplementary data to this article can be found online at https://doi.org/10.1016/j.desal.2023.116887.

CRediT authorship contribution statement

Jonathan Ehring: Conceptualization, Methodology, Validation, Formal analyses, Data curation, Writing – original draft, Review, & Edit, Visualization; Ali Vala Mizrak: Conceptualization, Writing- Original Draft preparation; Lutfi Agartan: Methodology, Writing - review, & edit; Bilen Akuzum: Methodology, Writing - review, & edit; E. Caglan Kumbur: Writing - review, & edit, Supervision.

Declaration of competing interest

The authors declare that they have no known competing financial interests or personal relationships that could have appeared to influence the work reported in this paper.

Data availability

Data will be made available on request.

Acknowledgments

The authors would like to thank the Graduate Assistantship for Areas of National Need (GAANN) and the National Science Foundation (Grant # 2034108) for supporting this work.

References

[1] W.-Y. Wu, et al., Divergent effects of climate change on future groundwater availability in key mid-latitude aquifers, Nat. Commun. 11 (2020) 3710.
[2] M. Qasim, et al., Reverse osmosis desalination: a state-of-the-art review, Desalination 459 (2019) 59–104.
[3] H.J. Chung, et al., Feasibility study of reverse osmosis-flow capacitive deionization (RO-FCDI) for energy-efficient desalination using seawater as the flow-electrode aqueous electrolyte, Desalination 479 (2020), 114326.
[4] M. McKague, et al., Extending pore network models to include electrical double layer effects in micropores for studying capacitive deionization, Desalination 535 (2022), 115784.
[5] X.T. Liu, et al., Cost comparison of capacitive deionization and reverse osmosis for brackish water desalination, ACS Es&T Eng. 1 (2) (2021) 261–273.
[6] S. Porada, L. Zhang, J.E. Dykstra, Energy consumption in membrane capacitive deionization and comparison with reverse osmosis, Desalination 488 (2020), 114383.
[7] M. Qin, et al., Comparison of energy consumption in desalination by capacitive deionization and reverse osmosis, Desalination 455 (2019) 100–114.
[8] L. Agartan, et al., Impact of flow configuration on electrosorption performance and energy consumption of CDI systems, J. Water Supply Res. Technol. AQUA 69 (2) (2020) 134–144.
[9] M.S. Alfonso, et al., Highly conductive colloidal carbon based suspension for flow-assisted electrochemical systems, iScience 24 (5) (2021), 102456.
[10] V.E. Brunini, Y.M. Chiang, W.C. Carter, Modeling the hydrodynamic and electrochemical efficiency of semi-solid flow batteries, Electrochim. Acta 69 (2012) 301–307.
[11] B. Akuzum, et al., Percolation characteristics of conductive additives for capacitive flowable (semi-solid) electrodes, ACS Appl. Mater. Interfaces 12 (5) (2020) 5866–5875.
[12] M.B. Dixit, et al., Mapping charge percolation in flowable electrodes used in capacitive deionization, ACS Mater. Lett. 1 (1) (2019) 71–76.
[13] L.Q. Xu, et al., Precise manipulation of the charge percolation networks of flow-electrode capacitive deionization using a pulsed magnetic field, Water Res 222 (2022), 118963.
[14] Y. Liu, et al., In situ synthesis of bismuth nanoclusters within carbon nano-bundles from metal–organic framework for chloride-driven electrochemical deionization, Adv. Funct. Mater. 32 (12) (2022) 2110087.
[15] L.H. Wang, et al., Up-shifting the desalination rate limit of capacitive deionization via integrating chloride-capturing Bi nanocluster with flow-through cell architecture, Chem. Eng. J. 460 (2023), 141726.
[16] K. Wang, et al., In situ synthesis of ultrasmall $NaTi_2(PO_4)_3$ nanocube decorated carbon nanofiber network enables ultrafast and superstable rocking-chair capacitive deionization, Chem. Eng. J. 463 (2023), 142394.
[17] Y. Liu, et al., Mn_2O_3 nanoflower decorated electrospun carbon nanofibers for efficient hybrid capacitive deionization, Desalination 494 (2020), 114665.
[18] H.-R. Park, et al., Surface-modified spherical activated carbon for high carbon loading and its desalting performance in flow-electrode capacitive deionization, RSC Adv. 6 (74) (2016) 69720–69727.
[19] C.R. Dennison, et al., Effects of flow cell design on charge percolation and storage in the carbon slurry electrodes of electrochemical flow capacitors, J. Power Sources 247 (2014) 489–496.
[20] K. Percin, et al., 3D-printed conductive static mixers enable all-vanadium redox flow battery using slurry electrodes, J. Power Sources 379 (2018) 228–233.
[21] K.Y. Chen, et al., Carbon nanotubes/activated carbon hybrid as a high-performance suspension electrode for the electrochemical desalination of wastewater, Desalination 522 (2022), 115440.
[22] Y. Cho, et al., Flow-electrode capacitive deionization with highly enhanced salt removal performance utilizing high-aspect ratio functionalized carbon nanotubes, Water Res. 151 (2019) 252–259.
[23] K.B. Hatzell, et al., Effect of oxidation of carbon material on suspension electrodes for flow electrode capacitive deionization, Environ. Sci. Technol. 49 (5) (2015) 3040–3047.
[24] C. Zhang, Evaluation of long-term performance of a continuously operated flow-electrode CDI system for salt removal from brackish waters, Water Res. 173 (2020), 115580.
[25] B. Akuzum, et al., Obstructed flow field designs for improved performance in vanadium redox flow batteries, J. Appl. Electrochem. 49 (6) (2019) 551–561.
[26] A. Heidarian, S.C.P. Cheung, G. Rosengarten, The effect of flow rate and concentration on the electrical conductivity of slurry electrodes using a coupled computational fluid dynamic and discrete element method (CFD–DEM) model, Electrochem. Commun. 126 (2021), 107017.
[27] J. Lohaus, et al., On charge percolation in slurry electrodes used in vanadium redox flow batteries, Electrochem. Commun. 101 (2019) 104–108.
[28] X.Y. Zhang, et al., Flow-electrode capacitive deionization utilizing three-dimensional foam current collector for real seawater desalination, Water Res. 220 (2022), 118642.
[29] F. Yang, et al., Decreased charge transport distance by titanium mesh-membrane assembly for flow-electrode capacitive deionization with high desalination performance, Water Res. 164 (2019), 114904.
[30] N.C. Hoyt, et al., Editors’ choice—electrochemical impedance spectroscopy of flowing electrosorptive slurry electrodes, J. Electrochem. Soc. 165 (10) (2018) E439–E444.
[31] A. Rommerskirchen, et al., Unraveling charge transport in carbon flow-electrodes: performance prediction for desalination applications, Carbon 145 (2019) 507–520.
[32] J.X. Ma, et al., Flow-electrode capacitive deionization (FCDI) scale-up using a membrane stack configuration, Water Res. 168 (2020), 115186.
[33] J.J. Chang, et al., Superiority of a novel flow-electrode capacitive deionization (FCDI) based on a battery material at high applied voltage, Desalination 468 (2019), 114080.

[34] Q. Wei, et al., Low energy consumption flow capacitive deionization with a combination of redox couples and carbon slurry, Carbon 170 (2020) 487–492.
[35] J. Wang, et al., The optimized flow-electrode capacitive deionization (FCDI) performance by ZIF-8 derived nanoporous carbon polyhedron, Sep. Purif. Technol. 281 (2022), 119345.
[36] S. Yang, et al., Analysis of the desalting performance of flow-electrode capacitive deionization under short-circuited closed cycle operation, Desalination 424 (2017) 110–121.